water

MDPI

Article

Drivers of Barotropic and Baroclinic Exchange through an Estuarine Navigation Channel in the Mississippi River Delta Plain

Gregg A. Snedden

Wetland and Aquatic Research Center, U.S. Geological Survey, Baton Rouge, LA 70803, USA; sneddeng@usgs.gov; Tel.: +1-225-578-7583

Academic Editor: Y. Jun Xu
Received: 26 February 2016; Accepted: 26 April 2016; Published: 30 April 2016

Abstract: Estuarine navigation channels have long been recognized as conduits for saltwater intrusion into coastal wetlands. Salt flux decomposition and time series measurements of velocity and salinity were used to examine salt flux components and drivers of baroclinic and barotropic exchange in the Houma Navigation Channel, an estuarine channel located in the Mississippi River delta plain that receives substantial freshwater inputs from the Mississippi-Atchafalaya River system at its inland extent. Two modes of vertical current structure were identified from the time series data. The first mode, accounting for 90% of the total flow field variability, strongly resembled a barotropic current structure and was coherent with alongshelf wind stress over the coastal Gulf of Mexico. The second mode was indicative of gravitational circulation and was linked to variability in tidal stirring and the horizontal salinity gradient along the channel's length. Tidal oscillatory salt flux was more important than gravitational circulation in transporting salt upestuary, except over equatorial phases of the fortnightly tidal cycle during times when river inflows were minimal. During all tidal cycles sampled, the advective flux, driven by a combination of freshwater discharge and wind-driven changes in storage, was the dominant transport term, and net flux of salt was always out of the estuary. These findings indicate that although human-made channels can effectively facilitate inland intrusion of saline water, this intrusion can be minimized or even reversed when they are subject to significant freshwater inputs.

Keywords: estuaries; salt transport; circulation; wavelet analysis; Mississippi River delta

1. Introduction

The quantity and distribution of salt in coastal waters is determined by the relative importance of the seaward mixing of relatively fresh upland drainage and the landward mixing of saline ocean water imported from shelf regions. These mixing processes can either be advective or dispersive. Advection occurs when salt is displaced by the net flow of water over the course of a tidal cycle, either through barotropic currents induced by gradients in water surface elevation such as those caused by wind or tidal forcing [1] or through baroclinic currents induced by longitudinal density gradients, which cause dense, saline water near an estuary's mouth to flow landward near the bottom, usually beneath a surface layer of relatively fresh, seaward-flowing water [2,3]. Dispersive processes occur when a net transport of salt occurs over a tidal cycle even though there is no net movement of water. One such process, tidal oscillatory salt flux, arises from correlations between depth-averaged velocity and salinity over the course of a tidal cycle that can occur if water flowing through a given cross section during the flood has a higher (or lower) salinity than that returning to sea on the ensuing ebb [3].

The manner and degree to which salt is imported to or exported from an estuary or transported within it can vary widely with fluctuations in river inputs, tidal amplitude, meteorological forcing,

and strength of the longitudinal salinity gradient. River inputs can affect an estuary's salt balance in multiple ways. If river flow is very large, a sea-level gradient can be induced in which ensuing barotropic currents can flush nearly all intruding saltwater out of an estuary [4]. On the other hand, moderate freshwater inflows can facilitate saltwater intrusion through the induction of longitudinal density gradients [5] along the estuarine channel that can drive baroclinic currents [6]. Fortnightly tidal amplitude variability can also regulate circulation and mixing processes. Baroclinic currents that become established during periods of low tidal amplitude (neap or equatorial tides) can be diminished or eliminated when tidal amplitude becomes large (spring or tropic tides) as turbulence generated at the channel bottom increases and propagates further up into the overlying water column, homogenizing the velocity field and reducing the bi-directional flow [7]. During these times dispersive processes such as tidal oscillatory salt flux can become more important in regulating an estuary's salt balance. Finally, meteorological forcing can force estuary-ocean exchange in two distinct ways. First, local wind stress (blowing directly over the estuary) transfers momentum from the atmosphere directly into the underlying water column, producing vertically-sheared currents. Second, remote winds (blowing outside the estuary over the adjacent shelf) can induce setup or setdown in the coastal ocean, and force barotropic exchanges driven by sea-surface slopes [8–12].

Saltwater intrusion is widely accepted as a significant contributor to the high rate at which the coastal wetlands situated on the Mississippi River delta plain in the northern Gulf of Mexico (GOM) have eroded and transitioned to open water [13–15], and the construction of straight, deep canals that connect saline shelf waters to interior marshes may have greatly exacerbated this problem [16]. Since the mid-1800 s, ten federal navigation canals have been constructed along the Louisiana coast, primarily to facilitate navigation associated with fossil fuel exploration and extraction activities. One such canal, the Houma Navigation Canal (HNC; Figure 1), was completed in 1962 and connects the Gulf Intracoastal Waterway (GIWW) near Houma, Louisiana, with the GOM near Cocodrie, Louisiana. Progressing inland from its seaward extent, the canal traverses saline, mesohaline and fresh marsh landscapes over its 45 km length. Since the HNC was completed, a gradual landward encroachment of mesohaline marsh into regions that were once fresh has been observed [17–21] and expansive areas of marsh have been converted to open water [22].

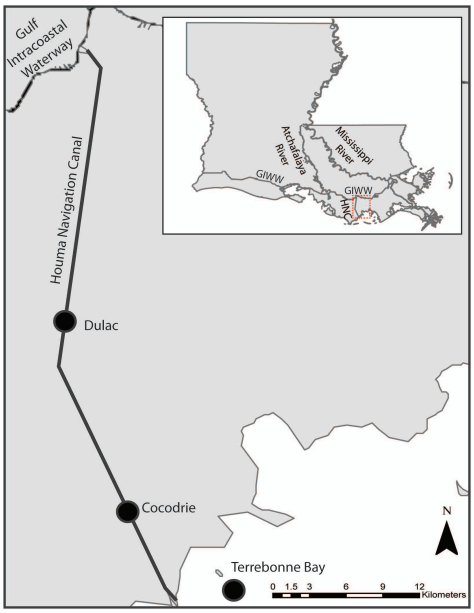

Figure 1. The Houma Navigation Canal (HNC) including the Cocodrie station where hourly velocity and wind time series measurements and tidal cycle hydrographic surveys were conducted. Horizontal salinity gradients were calculated as the difference between salinity at Terrebonne Bay and Dulac. Also shown are the Atchafalaya and Mississippi Rivers and the Gulf Intracoastal Waterway (GIWW).

Understanding how the circulation and mixing processes in estuarine navigation channels influence the exchange of salt between coastal wetlands and the coastal ocean, and how these processes are modulated by external physical processes is critical to anticipating the effects of future actions and circumstances on river deltas such as deepening or placing locks in navigation channels, changes in freshwater discharge, and sea level rise. This study investigates the variability in the velocity field and salt flux in the HNC and how wind forcing, buoyancy forcing, and mixing from tidal stirring may influence dispersive and advective fluxes through the HNC.

2. Materials and Methods

2.1. Study Site

The HNC is approximately 5 m deep and ranges between 50 and 100 m wide. Freshwater inputs to the HNC are strongly associated with discharge of the lower Atchafalaya River [23] (Figure 1). These inputs are conveyed to the HNC by way of the GIWW, and are typically highest during spring and early summer. In 2011, one of the largest flow events on record occurred on the Mississippi-Atchafalaya River system, during which the combined flow of the rivers exceeded 30,000 $m^3 \cdot s^{-1}$ for six weeks between May and June (Figure 2a). Sea level variability over the southeastern Louisiana continental shelf, which strongly influences barotropic exchanges between the estuary and the coastal ocean, occurs over a broad range of time scales. Astronomical tidal amplitudes are weak and diurnal, with the O_1 and K_1 constituents being the primary components of the tide. The importance of semi-diurnal constituents (e.g., M_2, S_2) in the overall astronomical tidal fluctuations along the northern and eastern coasts of the Gulf of Mexico is minimal. One important implication of the dominance of the diurnal constituents in this region is that the fortnightly cycle in tidal amplitude results from an offset of the plane of the moon's orbit relative to the earth's equator. This 13.6-day tropic-equatorial cycle is physically distinct from the 14.8-day spring-neap fortnightly cycle in tidal amplitude that occurs in semi-diurnal regimes as a result of varying positions of the sun and the moon relative to the earth. Over timescales of a few days, wind stress becomes important in regulating estuary-shelf exchanges, particularly during autumn and winter when the passage of winter storm systems occurs every 4–7 days [24] and causes shelf sea levels to fluctuate with typical amplitudes of approximately 0.5 m.

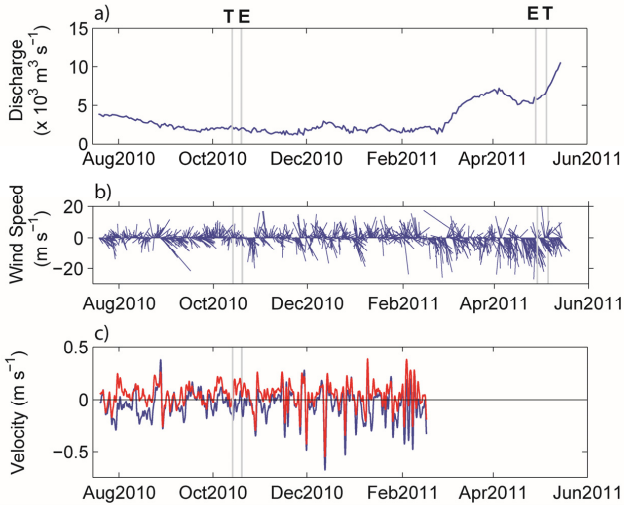

Figure 2. (**a**) Lower Atchafalaya River discharge at Morgan City, Louisiana; (**b**) Wind speed and direction at Dulac, Louisiana. Length of vector indicates speed of wind; angle of vector denotes direction from which the wind is blowing; (**c**) Near-surface (blue) and near bottom (red) current velocity in the Houma Navigation Canal at Cocodrie, LA. Positive values denote landward flow; negative values denote seaward flow. The gray vertical lines indicate tidal cycle sampling events during tropic (**T**) and equatorial (**E**) phases of the fortnightly cycle.

2.2. Data Collection

Hourly time series measurements of vertical current velocity profiles were made with a 1500 kHz Sontek acoustic Doppler current profiler (ADCP) from July 2010 through February 2011 at a fixed station (Cocodrie; Figure 1). Hourly wind velocity and near-surface salinity measurements were also taken at Dulac during this time period. The difference in salinity between Terrebonne Bay and Dulac (Figure 1) was used to calculate the horizontal salinity gradient at Cocodrie. All time series were passed through a Lanczos filter [25] with a half-amplitude cutoff period of 33 h to remove tidal variability from the records. Current velocity data were defined as positive flowing landward. Wind velocity data were used to calculate wind stress following Large and Pond [26], and defined as positive toward east and north for along- and cross-shelf winds, respectively.

Vertical profiles of hydrographic properties and current velocity were collected hourly over complete diurnal tidal cycles (25h) at Cocodrie with a Sontek CastAway conductivity-temperature-depth (CTD) profiler and a Sontek RiverSurveyor M9 boat-mounted ADCP (Figure 1). This sampling was conducted during low (autumn 2010) and high (spring 2011) Atchafalaya River flow conditions (Figure 2, top panel) during tropic (13–14 October 2010; 5–6 May 2011) and equatorial (19–20 October 2010; 28–29 April 2011) phases of the fortnightly tidal cycle.

2.3. Data Analysis

Though cross-Fourier [27] analysis is widely used to examine co-variability in geophysical time series, cross-wavelet [28,29] analysis was used here because it is better-suited for situations where variance in the component signals may be localized in time [30]. One particular wavelet, Morlet, is defined as

$$\psi_o(\eta) = \pi^{-1/4} e^{i\omega_o \eta} e^{-\frac{1}{2}\eta^2} \tag{1}$$

where ω_o is dimensionless frequency and η is time. This wavelet consists of a complex wave ($e^{i\omega\eta}$) within a Gaussian filter ($e^{-\frac{1}{2}\eta^2}$) which localizes the amplitude of the wavelet in time. The wavelet transform of a time series x_n ($n = 1, \ldots, N$) with time steps δt is the convolution of x_n with the scaled and normalized wavelet,

$$W_n^x(s) = \sqrt{\frac{\delta t}{s}} \sum_{n'=1}^{N} x_n \psi \left[(n' - n) \frac{\delta t}{s} \right] \tag{2}$$

where s is timescale. Similar to Fourier analysis, the wavelet power spectrum is taken as $|W_n^x|^2$. In simple terms, the wavelet spectrum provides an estimate of variance for a time series as a function of time and timescale (period) of variability. It does so by estimating localized sinusoidal variance over varying timescales throughout the duration of the time series.

Because the length of time series records is finite, errors occur at the left and right regions of the wavelet spectrum. To cope with boundary effects of finite time series, each end of the time series is padded with zeroes. This procedure introduces discontinuities and decreases variance at the ends of the time series, and the region of the wavelet spectrum where these issues occur is termed the cone of influence. Caution should be made in these regions as it can be unclear whether decreases in wavelet power are due to true decreases in the signal variance or are simply artifacts of zero padding.

Similar to cross-Fourier analysis [27], the cross-wavelet spectrum of two time series x_n and y_n can be defined as $W^{XY} = W^X W^{Y*}$, where * denotes the complex conjugate of the preceding quantity. The cross-wavelet transform can then be used to compute the wavelet coherence, which indicates the localized correlation between two time series in time-frequency space, estimated as

$$R^2(t,s) = \frac{\left| \langle s^{-1} W^{XY}(t,s) \rangle \right|^2}{\langle s^{-1} \left| W^X(t,s) \right|^2 \rangle \langle s^{-1} \left| W^Y(t,s) \right|^2 \rangle} \tag{3}$$

where $\langle\ \rangle$ indicates smoothing in both time and scale. Bearing in mind that Equation (3) closely resembles that of a time-domain correlation coefficient, it is useful to consider it as a localized coefficient of determination in time-frequency space. Also similar to cross-Fourier analysis, the wavelet phase spectrum can be estimated as

$$\varphi_{xy}(t,s) = \tan^{-1}\left(\frac{Im\left\{s^{-1}W^{XY}\right\}}{Re\left\{s^{-1}W^{XY}\right\}}\right) \tag{4}$$

where *Im* and *Re* indicate the imaginary and real components, respectively, of the following quantities. The phase spectrum provides an indication of the relative timing of the two time series in question, that is, by how much y_n leads or lags x_n.

In situations where two forcing mechanisms were examined simultaneously to determine their influence on a single response variable, a two-input partial wavelet model was used. This procedure entailed generalizing the approach described above to a two-input, one-output Fourier system [27], where Fourier and cross-Fourier spectra were replaced with their corresponding wavelet and cross-wavelet spectra.

The sampling depths z for velocity and salinity profiles obtained in the tidal cycle measurements were normalized to nondimensional values $Z = z/h(t)$, where $h(t)$ is the water depth at sampling time (t) [31]. The velocity vectors measured by the boat-mounted ADCP were decomposed into the along-channel (u) component with the x-axis oriented positively inland from the GOM. Salinity and velocity were interpolated along the water column at intervals of $0.1Z$.

Water column stability during each tidal cycle sampled was quantified through calculation of the layer Richardson number (Ri_L; [3]), defined as

$$Ri_L = \frac{gh\Delta\rho}{\overline{U}^2\overline{\rho}} \tag{5}$$

where $h = h(t)$ is the local depth, $\overline{\rho}$ is the mean density of the water column, $\Delta\rho$ is the difference between near-bottom and near-surface density and $\overline{U}$=$\overline{U}(t)$ is root-mean-square of the water column velocity. $Ri_L > 20$ indicates strong water column stability with negligible mixing. When $2 < Ri_L < 20$, the water column is weakly stable and moderate mixing occurs, while $Ri_L < 2$ indicates isotropic turbulence and fully-developed mixing. Using these thresholds, ($2 < Ri_L < 20$) allows for the comparison of vertical water column stability between measurement events.

To understand how the relative importance of various advective and dispersive processes varied under fluctuating degrees of wind, tidal and buoyancy forcing, the salt flux was decomposed [32] such that the total subtidal salt flux F through a given unit width of cross-section normal to the longitudinal flow is given by

$$F = \left\langle \int us\, dz \right\rangle \tag{6}$$

where $\langle\ \rangle$ denotes time-averaging over a tidal cycle, u is the along-channel velocity (positive flowing inland), s is salinity and z is water column depth at the Cocodrie survey location. The total salt flux can then be decomposed as

$$F = \left\langle \int (u_0 + u_E + u_T)(s_0 + s_E + s_T)\, dz \right\rangle \approx \left\langle \int (u_0 s_0 + u_E s_E + u_T s_T)\, dz \right\rangle = F_0 + F_E + F_T \tag{7}$$

where u and s are decomposed into tidally and depth averaged (u_0, s_0), tidally averaged and depth varying (u_E, s_E), and tidally and depth-varying (u_T, s_T) components. Each term in (7) refers to a specific physical process. The first term F_0 is the salt flux owing to the subtidal depth-averaged (barotropic) transport, including salt loss due to river discharge and subtidal salt flux (storage and release) due to wind-forced estuary-shelf exchange. The second term F_E is the subtidal shear dispersion resulting from gravitational circulation, which advects saline water upestuary near the bottom and relatively fresh

water downestuary near the surface. Thus, its net contribution is usually downgradient (upestuary). The third term F_T is the tidal oscillatory salt flux resulting from temporal correlations between u_T and s_T. Because currents and salinity vary approximately sinusoidally over a tidal cycle, the magnitude of this term is to some degree a function of the phase differences between the two variables. This term will be large if the currents and salinity vary in phase with each other, and will be negligible if the two terms are in quadrature phase (*i.e.*, maximum salinity occurs during slack currents at the end of the flood tide). This flux is usually directed landward, but not always.

3. Results and Discussion

3.1. Vertical Variation in Subtidal Velocity Dtructure at Cocodrie

Winds were generally light and variable through mid-September, 2010, and then increased in intensity and turned predominantly southward by late October. The passage of several winter frontal systems is evident between this time and the remainder of the data collection period (February 2011; Figure 2b). Subtidal current velocity magnitudes generally did not exceed 0.4 m·s^{-1}, and though the currents appeared to be largely depth-independent, there were several brief episodes where considerable vertical current shear was evident (Figure 2c).

Empirical orthogonal function (EOF) analysis [33] was performed on the Cocodrie current velocity data set to provide a compact description of the dominant modes of vertical variation of currents in the lower HNC. EOF analysis optimally partitions the variance of a field into orthogonal patterns or modes (vertical modes, in this case) that are simply the eigenvectors of the data field's covariance matrix. Each mode is associated with a corresponding eigenvalue that is proportional to its percentage of the total variance in the dataset. Each mode is also associated with a time series (principal component; PC) that describes the EOF's evolution through time. EOF solutions were normalized to their standard deviations, giving each principal component time series a non-dimensional variance of unity and, thus, the eigenvectors carry units in m· s^{-1} (positive values indicate landward flow).

The first two EOF modes accounted for 99.6% of the total subtidal flow variability at Cocodrie. Over 90% of the total variability could be attributed to mode 1, which carries the same sign (negative) throughout the water column, with a slight magnitude decrease with increasing depth (Figure 3a). Hence, mode 1 depicts currents at Cocodrie in which the direction of the flow does not vary with depth, and appears to represent barotropic exchanges (driven by sea-surface elevation gradients) that occur in the lower HNC between Terrebonne Bay and the wetlands to its north. Mode 2 accounted for slightly greater than 8% of the total flow field variability. Unlike mode 1, a reversal in sign at roughly mid-depth exists in the eigenvector for mode 2 (Figure 3c), and mode 2 hence represents flow where the surface currents opposed those at the bottom. None of the remaining eight modes comprise greater than 0.2% of the total flow field variability.

Current velocities throughout the water column at a particular time associated with a given EOF mode can be recovered by taking the product of the mode's eigenvector and principal component time series. Thus, bearing in mind that the current velocity data are defined as positive flowing inland, positive values for the time series describing the temporal evolution of the mode1 response (PC1) indicate outflows and negative values indicate inflows at Cocodrie (Figure 3b).

A two-input partial wavelet coherence model,

$$\hat{PC1} = a\hat{\tau}_x + b\hat{t}_y + \hat{\varepsilon} \tag{8}$$

was used to investigate the roles of along- (τ_x) and cross-shelf (τ_y) wind stress in forcing barotropic exchanges (PC1) through the HNC at Cocodrie, where the circumflex indicates the wavelet transform of the corresponding variable, a and b are complex transfer functions relating τ_x and τ_y to PC1, and ε is noise or residual error. The proportion of PC1 wavelet power explained by the two inputs together as a function of time and period is given by the multiple wavelet coherence spectrum.

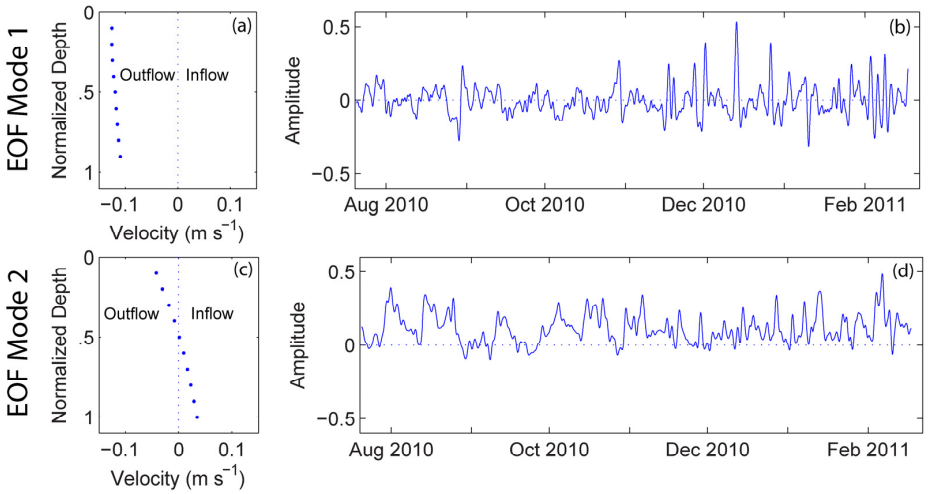

Figure 3. Vertical distributions of EOF eigenvectors (**a**,**c**); and principal component time series (**b**,**d**) for EOF modes 1 and 2 at Cocodrie. Positive eigenvector values indicate landward flow; negative values indicate seaward flow.

The wavelet spectra for τ_x and τ_y are similar (Figure 4a,b), with much of their variance concentrated in the 3–10 day band between November 2010 and February 2011. The wavelet spectrum of PC1 (Figure 4c) strongly resembles the spectra of the two wind stress components in that it also exhibits high variability over 3–10 day timescales during the winter months of the deployment. The partial wavelet coherence spectrum for τ_x and PC1 (Figure 5a) shows a region of high coherence over 3–10 day timescales across the latter portion of the record, a region where both time series show high variability. The phase in this region is near zero, indicating that winds blowing toward the east ($\tau_x > 0$) were associated with barotropic outflows (PC1 > 0) in the HNC at Cocodrie. Coherence over similar timescales existed between τ_y and PC1 from July to October, 2010 (Figure 5b). Phase in this region of time-frequency space was near 180°, indicating that winds blowing toward the north ($\tau_y > 0$) were associated with barotropic inflows (PC1 < 0). The multiple wavelet coherence spectrum exceeds 0.9 across a very large portion of time-frequency space (Figure 5c)- particularly the region where PC1 was most energetic, indicating that barotropic estuary-ocean exchanges at Cocodrie are driven almost entirely by fluctuations in the two orthogonal wind stress components.

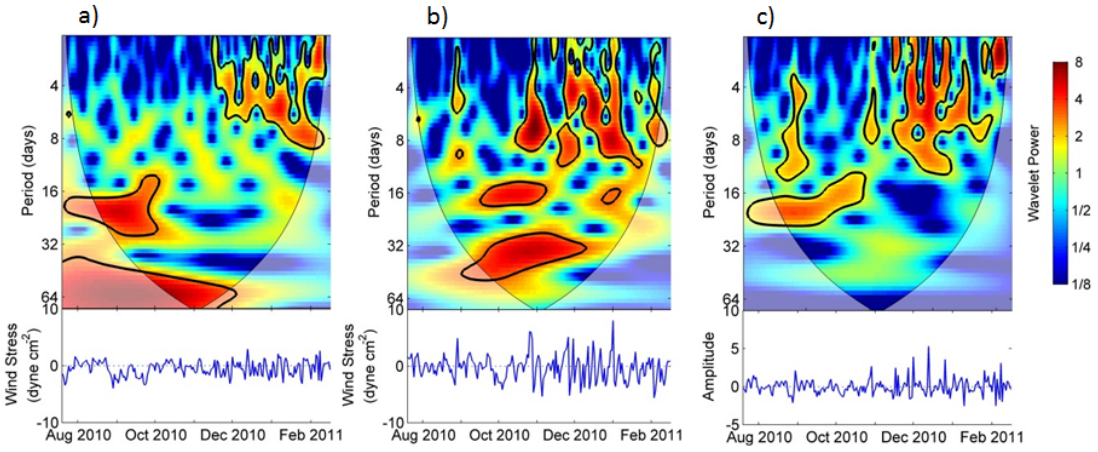

Figure 4. Wavelet power spectra (top) and time series plot (bottom) of along-shelf wind stress (**a**; τ_x); cross-shelf wind stress (**b**; τ_y); and PC1 (**c**). Wavelet power is normalized by the variance of each time series.

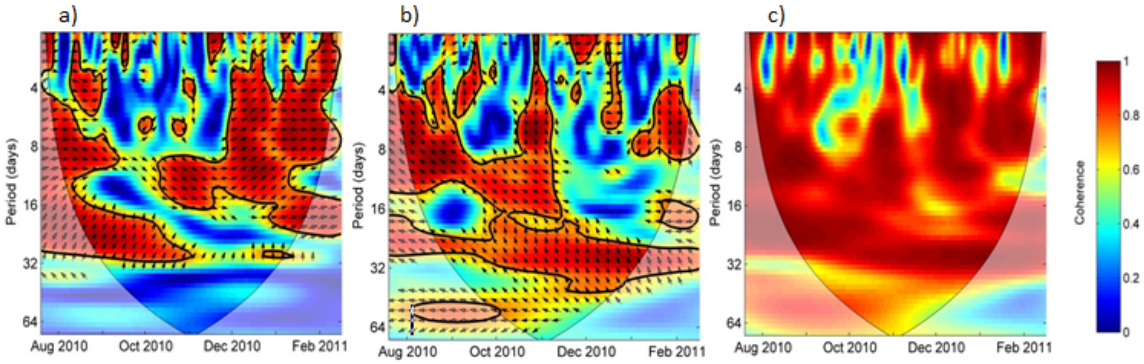

Figure 5. Partial wavelet coherence and phase spectra of along-shelf (**a**; τ_x) and cross-shelf (**b**; τ_y) wind stress with PC1. Solid lines delineate regions of time-frequency space where coherence between the time series is significant at $\alpha = 0.05$. Phase is indicated by the direction of the arrows, where an arrow pointing toward the right indicates an in-phase (positive with little or no time lag) relation, an arrow pointing down indicates PC1 lags wind stress by 90°, and arrow to the left indicates the two time series are out of phase by 180° (inverse relation with little or no lag) and an upward pointing arrow indicates PC1 leads wind stress; (**c**) Multiple wavelet coherence spectrum of τ_x and τ_y with PC1.

The time series describing the temporal pattern of the sheared flow response (PC2) nearly always carries a positive sign (Figure 3d), Thus, flows associated with mode 2 can be characterized by outflow (negative velocity) in the upper water column with inflows (positive velocity) near the bottom, and resemble what one might expect from traditional baroclinic estuarine circulation theory. The relative roles of variability in diurnal tidal current amplitude A_{tid} and horizontal salinity gradient ΔS in regulating baroclinic exchanges at Cocodrie (PC2) were investigated with a two-input partial wavelet model,

$$\hat{PC2} = m\hat{A}_{tid} + n\hat{\Delta S} + \hat{\varepsilon} \quad (9)$$

where A_{tid} was estimated with complex demodulation [25]. Here, m and n are transfer functions relating A_{tid} and ΔS to PC2.

The amplitude of the diurnal tidal current varied between 10 and 40 cm·s^{-1}, and showed a clear fortnightly cycle, with a recurrence interval very close to the 13.6-day tropic-equatorial cycle (Figure 6a). The horizontal salinity gradient is always positive, indicating higher salinities in shelf waters than in the estuary, and its magnitude shows considerable variability, pulsing every 10–25 days during the early and latter portions of the record (Figure 6b). The wavelet power spectrum for PC2 strongly resembles that of ΔS, with elevated variance across timescales of 10–25 days from July through October (Figure 6c). The variability over this time scale then diminishes through early January, and then returns for the remainder of the record.

The partial wavelet coherence spectrum between A_{tid} and PC2 (Figure 7a) indicates that these two variables were coherent over fortnightly timescales, close to the 13.6-day tropic equatorial period. Phase in this region is near 180°, indicating that two-layer flow is inhibited when tidal currents are strong. Strong coherence also exists between ΔS and PC2, primarily over timescales of 10–25 days between July and November 2010 (Figure 7b). Phase in the highly coherent regions is near 0°, with PC2 variability slightly lagging that of the horizontal density gradient, suggesting that increases in the horizontal density gradient were followed by enhanced two-layer circulation in the HNC at Cocodrie. The multiple wavelet coherence spectrum is greater than 0.8 throughout a wide region of time-frequency space, suggesting the two inputs adequately explain the variability of PC2. Together, results of the two-input partial wavelet model illustrate that gravitational circulation is strongest when the horizontal salinity gradient is large during equatorial tides (weak tidal currents).

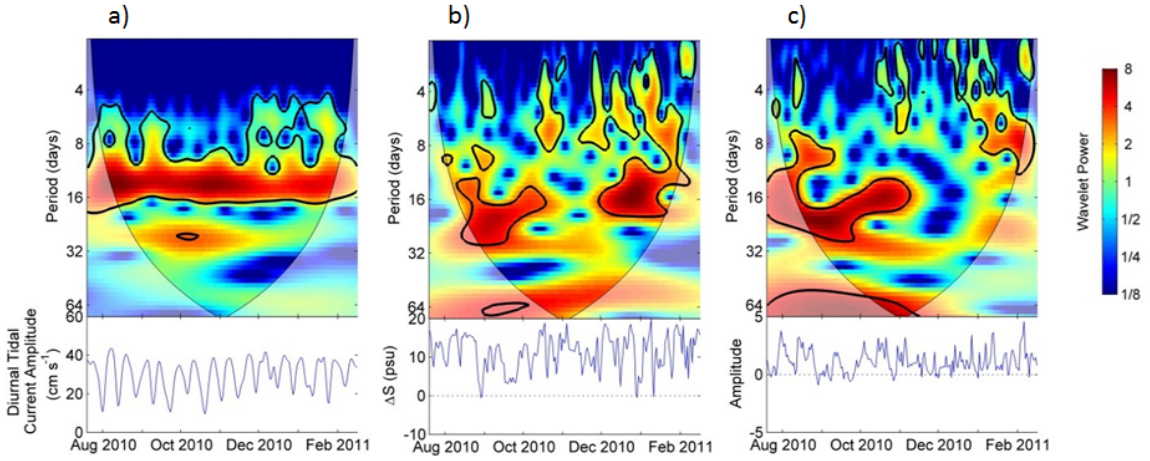

Figure 6. Wavelet power spectra (top) and time series plot (bottom) of diurnal tidal current amplitude (**a**; A_{tid}); the horizontal salinity gradient (**b**; ΔS); and PC2 (**c**).

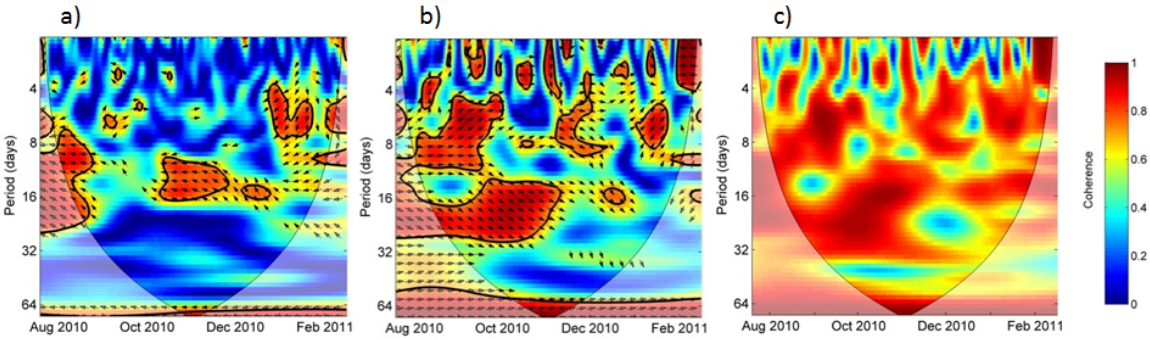

Figure 7. Partial wavelet coherence and phase spectra of diurnal tidal current amplitude (**a**; A_{tid}); the horizontal salinity gradient (**b**; ΔS); and (**c**) with PC2. Multiple wavelet coherence spectrum of A_{tid} and ΔS with PC2.

EOF analysis was effective in decomposing the vertical structure of the subtidal current velocity data into two dominant modes of variability that accounted for greater than 99% of the total variance at Cocodrie. The flow was predominantly barotropic, and bottom friction was evident in this mode, as indicated by the slight amplitude reduction in the mode 1 eigenvectors near the bottom of the water column (Figure 3a). Observational studies have well documented that alongshore wind stress plays a key role in facilitating barotropic estuary-shelf exchange through the induction of sea level slopes at the estuary-ocean interface by Ekman convergence/ divergence [8–12], and these dynamics have also been simulated with numerical modeling [34–36]. Alongshore winds blowing outside of Breton Sound, Louisiana, were much more effective at influencing water level variability that resulted from changes in storage than winds blowing either across the shelf or along the length axis of the estuary; the weak response to cross-shelf, along-estuary wind stress was attributed to limitations in fetch across the relatively shallow, complex deltaic landscape [37]. Similarly, alongshore winds blowing toward east were found to be effective in forcing barotropic outflows from Barataria Bay to the Gulf of Mexico through Barataria Pass, whereas westward wind stress forced inflows of Gulf waters into the bay through the pass [38]. Though barotropic exchanges were also coherent with cross-shelf wind forcing in the early part of the study (Figure 5b), the response amplitude in exchange flows to cross-shelf wind forcing appears to be minimal, as indicated by the relatively low variance in the PC1 wavelet spectrum during this time. A simple one-dimensional barotropic analytical model [39] applied to coastal bays in Louisiana revealed that in this region cross- and alongshore wind stress can be equally effective in

driving subtidal volume exchanges between the bays and the Gulf of Mexico [40]. Model simulations of Perdido Bay Estuary, Alabama, showed water outflow from the estuary to the coastal ocean was most strongly associated with offshore (southward) winds [41].

Mode 2 was characterized by strong vertical shear in flow, with the upper layer of the water column always flowing seaward and opposite to that of the lower layer. No substantial reversals in this pattern occurred during the period of data collection at Cocodrie and thus, mode 2 appears to be gravitationally-driven estuarine exchange flow, and this exchange flow responded strongly to variations in the longitudinal salinity gradient. The dependence of gravitational circulation on the longitudinal density gradient has been described analytically by [2], and numerous observational studies have documented this response, where enhanced density gradients drove stronger gravitational circulation [42] or even reversed it in the case of inverse estuaries where estuarine salinities exceeded those in shelf waters [43–47].

An inverse relation between the strength of the baroclinic exchange and tidal amplitude observed here was observed in Puget Sound [48], in which a twofold variation in the strength of the exchange flow at the entrance to Puget Sound occurred over the course of the fortnightly tidal cycle, with maximum exchange flow occurring during neap tide and minimum during spring. In Bertioga Channel, Brazil, upstream salt transport driven by gravitational circulation was observed to exceed that of tidal salt flux by a factor of 2.7 during neap tides, while during spring tides the tidal flux term exceed gravitational circulation by a factor of 1.4 [49]. In Barataria Pass, Louisiana, a 101-day ADCP record revealed that baroclinic currents were strongly coupled with tidal current amplitudes over fortnightly timescales, with greatest velocity shear occurring during equatorial tides when current amplitude was minimal [38]. These observational findings have been corroborated numerically, where order-of-magnitude reductions in vertical diffusivity have been found to occur following the transition from spring to neap tides [50], and also with physical models, where inverse relations between tidal amplitude and vertical salinity stratification have been documented for Chesapeake Bay [51].

3.2. Tidal Cycle Salinity and Velocity Surveys and Salt Flux Decomposition

The salinity field over the equatorial tide sampled during low Atchafalaya River flow (October 2010) was strongly stratified, whereas the velocity field was much more vertically homogenous (Figure 8). Layer Richardson numbers during the equatorial tide generally were near or exceeded 20 (Figure 9), indicating there was insufficient turbulent energy in the water column to mix the surface and bottom layers. Salinity stratification in the autumn low-flow period during the tropic tide was reduced (Figure 8), likely a result of more vigorous vertical mixing of water due to increased tidal stirring power as a result of the elevated current velocities, and these conditions were generally reflected in the reduced layer Richardson numbers (Figure 9).

Vertical structure of salinity and velocity at Cocodrie was strongly influenced by high river flow during the spring 2011 tidal cycle sampling events. Flow was predominantly ebb-directed during the entirety of both tidal cycles that were sampled, and the stratification observed during the autumn 2010 equatorial tide survey was almost nonexistent during the spring 2011 survey (Figure 8). During this time, Atchafalaya River discharge (6200 $m^3 \cdot s^{-1}$) was over threefold what it was during the October survey (2000 $m^3 \cdot s^{-1}$; Figure 2a), and the resulting high freshwater inputs to the HNC flushed much of the salt out of the HNC, which may have precluded any significant stratification from occurring. The reduced stratification during the spring sampling events may also be a reflection of increased stirring power brought about by high outflow velocities associated with the high river flow. These conditions are well-reflected by the layer Richardson numbers (Figure 9), which are considerably lower than those calculated for low river flow conditions and are nearly always less than 20, the upper limit for Ri_L for which turbulent mixing near the pycnocline can be expected to occur in partially mixed estuaries [52,53].

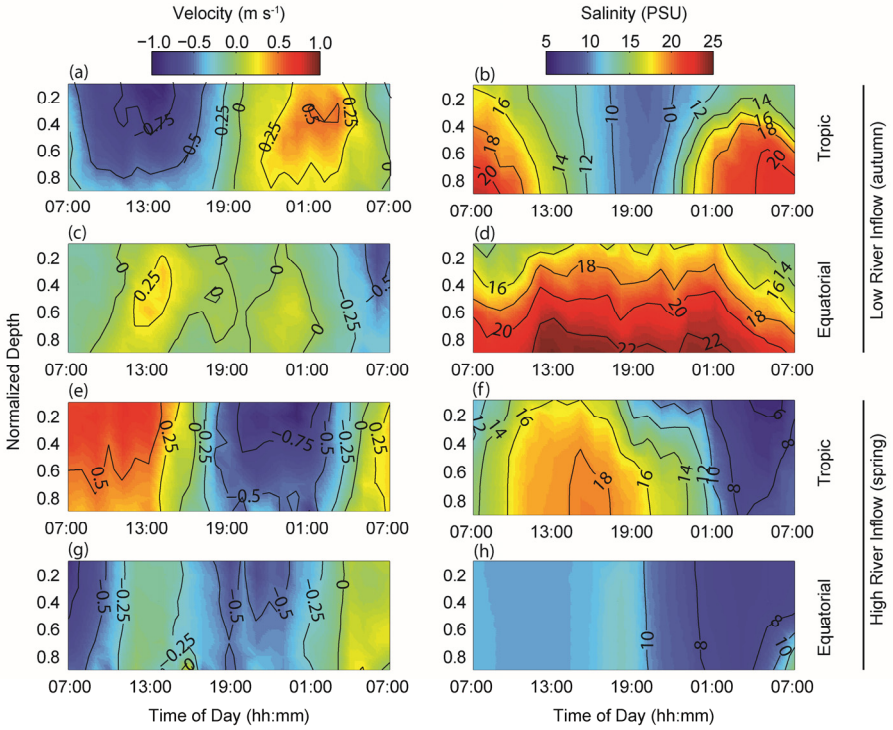

Figure 8. Intratidal variation of vertical current (**a**,**c**,**e**,**g**) and salinity (**b**,**d**,**f**,**h**) profiles collected under high and low river inflow conditions during tropic and equatorial tides. Positive velocity values indicate landward flow, negative values denote seaward flow.

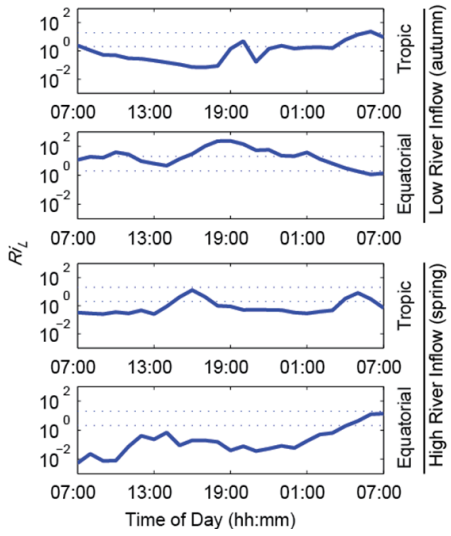

Figure 9. Layer Richardson numbers (Ri_L) during each of the tidal cycle surveys at Cocodrie. The dotted lines (Ri_L equal 2 and 20) indicate the upper limit for complete mixing and lower limit for full stratification, respectively. Between these limits water column stability is transitional.

Although tidal oscillatory flux (F_T) accounted for 65% of the upstream salt transport during the low river flow (Oct 2010) tropic tide, gravitational circulation (F_E) became the dominant transport mechanism during the following equatorial tidal cycle one week later, accounting for 74% of upstream transport. F_E was essentially non-existent high river flow (April–May 2011; Table 1). Strong upestuary winds that preceded this survey may provide one explanation. Upestuary winds have been observed to be particularly effective in decreasing salinity stratification, owing to two physically distinct

mechanisms. First, they drive a two-layer circulation that opposes gravitational circulation, in which surface currents flow into the estuary in the same direction as the wind and near-bottom currents return water to the ocean. Additionally, the water column is mixed through direct wind mixing, where turbulence generated at the air-sea interface is transferred down through the water column [54].

Table 1. Salt fluxes (kg· m^{-1}· s^{-1}) at Cocodrie during the four tidal cycles examined.

Salt Flux Term	Low River Flow		High River Flow	
–	Tropic	Equatorial	Tropic	Equatorial
Net ($\langle \int us\, dz \rangle$)	−2.35	−0.77	−0.14	−2.92
Advective (F_0)	−2.46	−1.05	−0.74	−3.04
Gravitational (F_E)	0.05	0.20	0.01	0.01
Tidal Oscillatory (F_T)	0.08	0.07	0.55	0.14
Balance (Net-[F_0 + F_E + F_T])	−0.02	0.01	0.03	−0.03

During all tidal cycles sampled, the dominant salt transport term was F_0 (Table 1), indicating that fluxes of salt were primarily driven by a combination of freshwater discharge through the HNC and wind-driven changes in storage over the course of the tidal cycle. The F_0 term was particularly large during the equatorial tidal cycle during high Atchafalaya River flow (28–29 April 2011). This large flux may have resulted from the release of water that entered the Terrebonne marshes surrounding the HNC in the preceding days as a result of very strong southeasterly winds. These winds ceased in the hours prior to the synoptic survey, possibly allowing for this stored water (and entrained salt) to be released from the Terrebonne marshes back into the HNC where it was conveyed to the coastal ocean as sampling was occurring. A tendency for F_0 to be the dominant salt transport term may exist in shallow, wind-driven microtidal systems such as those on the Mississippi River delta plain. In these settings, weak tidal currents combined with turbulent flows associated with shallow water depths may limit landward flux contributions from F_E and F_T to the overall salt balance, and may partially explain why the HNC was exporting salt during all sampling periods, as indicated by the negative value for the net transport term (Table 1). The observed net seaward fluxes may also be an indication that the assumption of lateral homogeneity, which must be made when sampling at a central point in the channel cross-section such as in the effort conducted here, was an inaccurate depiction of conditions throughout the entire channel cross-section.

4. Conclusions

The import of saline shelf waters into the HNC and their subsequent transport up the HNC channel occur primarily through wind-driven barotropic currents driven by alongshore wind stress over shelf waters adjacent to Terrebonne Bay. This finding was supported by results from the EOF analysis at Cocodrie, where the mode 1 vertical flow pattern resembled a depth-independent barotropic structure and accounted for greater than 90% of the flow variability at that location. The amplitude time series of this flow, measured by PC1 obtained from the EOF analysis, was most responsive to alongshore winds, and the near-zero phase between alongshore winds and PC1 indicates that winds blowing toward the east tend to precede barotropic outflows. These results are consistent with Ekman convergence/divergence at the coastal ocean, where winds blowing toward east tend to push water 90 degrees to the right (toward south and away from the coast), inducing a sea surface pressure gradient that leads to outflow from the HNC. The opposite occurs when winds blow toward the west-water is pushed against the coast and subsequently flows up into the HNC in response to the induced pressure gradient. Barotropic exchanges lead to changes in storage in the HNC and the surrounding marshes by introducing or removing seawater from the estuary.

The salt flux decomposition results indicate that F_0 is the dominant salt flux term, though less so during equatorial tides that occur during periods of low river flow. Under such conditions, salt flux brought about by gravitational circulation (F_E) becomes increasingly important. These results are

corroborated by the cross-wavelet analysis that examined coherence of tidal current with PC2, which indicated that brief spikes in baroclinic currents tended to occur during periods of low tidal amplitude, and that these baroclinic currents were enhanced if sufficient longitudinal salinity gradients were present. Though most existing studies show gravitational circulation to be enhanced during increased river flow, the opposite was observed in this study, possibly because the river flow in the spring 2011 tidal cycle sampling was so great that nearly all the salt was pushed out of the channel and turbulence generated at the channel bed was extremely high due to the unusually high velocities associated with such a large flood event. The tidal oscillatory flux term (F_T) tended to be most important during tropic tides, when tidal excursion distances were greatest and entrained salt particles could be transported furthest by tidal currents. The net salt flux term F_0 during all tidal cycles sampled indicates that the assumption that estuarine navigation channels on the Mississippi River delta are conduits for saltwater intrusion may not always hold true, particularly when these channels are directly or indirectly linked to sources of freshwater. Thus, further investigations of salt flux through the HNC and similar channels should be undertaken before major engineering endeavors such as lock installations are made for the purpose of increasing the resilience and sustainability of the deltaic landscape.

Acknowledgments: This study was funded in part by the U.S. Geological Survey and the Bureau of Ocean Energy Management. Holly Beck provided assistance with the figures in this manuscript. Erick Swenson provided a critical review of an earlier version of this manuscript. Thanks to Michael Descant, Brett Patton, David Heckman, Michael Bell, Todd Baumann, Paul Frederick, Lane Simmons, Errol Meche, Calvin Jones, Van Bergeron, and Garron Ross for assistance in the field. Any use of trade, firm, or product names is for descriptive purposes only and does not imply endorsement by the U.S. Government.

Author Contributions: G.S. conceived and designed the study, collected the field data, conducted data analysis, and wrote the article.

Conflicts of Interest: The author declares no conflict of interest.

Reference

1. Weisburg, R.H. The nontidal flow in the Providence River of Narragansett Bay: A stochastic approach to estuarine circulation. *J. Phys. Oceanogr.* **1976**, *9*, 721–734. [CrossRef]
2. Officer, C.E. *Physical Oceanography of Estuaries and Associated Coastal Waters*; John Wiley and Sons: New York, NY, USA, 1976.
3. Dyer, K.R. *Estuaries: A Physical Introduction*; John Wiley and Sons: New York, NY, USA, 1973.
4. Geyer, W.R. Tide-induced mixing in the Amazon frontal zone. *J. Geophys. Res. Oceans* **1995**, *100*, 2341–2353. [CrossRef]
5. Hansen, D.V.; Rattray, M. Gravitational circulation in straits and estuaries. *J. Mar. Res.* **1965**, *23*, 104–122.
6. Horn, D.A.; Laval, B.; Imberger, J.; Findikakas, A.N. Field study of physical processes in Lake Maracaibo. In Proceedings of the Congress international Association for hydraulic Research; Li, G., Ed.; Tsinghua University Press: Beijing, China, 2001; pp. 282–288.
7. Griffin, D.A.; Leblond, P.H. Estuary-ocean exchange controlled by spring-neap tidal mixing. *Estuar. Coast. Shelf Sci.* **1990**, *30*, 275–297. [CrossRef]
8. Elliott, A.J.; Wang, D.P. The effect of meteorological forcing on the Chesapeake Bay: The coupling between an estuarine system and its adjacent coastal waters. In *Hydrodynamics of Estuaries and Fjords*; Nihoul, J.C.J., Ed.; Elsevier: Amsterdam, The Netherlands, 1978; pp. 127–145.
9. Wang, D.P. Subtidal sea level variations in the Chesapeake Bay and relations to atmospheric forcing. *J. Phys. Oceanogr.* **1979**, *9*, 413–421. [CrossRef]
10. Wong, K.C. Sea level variability in Long Island Sound. *Estuaries* **1990**, *13*, 362–372. [CrossRef]
11. Wong, K.C.; Moses-Hall, J.E. On the relative importance of the remote and local wind effects to the subtidal variability in a coastal plain estuary. *J. Geophys. Res. Oceans* **1988**, *89*, 18393–18404. [CrossRef]
12. Janzen, C.D.; Wong, K.C. Wind-forced dynamics at the estuary-shelf interface of a large coastal plain estuary. *J. Geophys. Res. Oceans* **2002**, *107*, 1–12. [CrossRef]
13. Smart, R.M.; Barko, J.W. Nitrogen nutrition and salinity tolerance of Distichlis spicata and Spartina alterniflora. *Ecology* **1980**, *61*, 630–638. [CrossRef]

14. Linthurst, R.A.; Seneca, E.D. Aeration, nitrogen and salinity as determinants of *Spartina. alterniflora* Loisel. growth response. *Estuaries* **1981**, *4*, 53–63. [CrossRef]
15. Howard, R.J.; Mendelssohn, I.A. Salinity as a constraint on growth of oligohaline marsh macrophytes I: Species variation in stress tolerance. *Am. J. Bot.* **1999**, 785–794. [CrossRef]
16. Turner, R.E. Wetland loss in the northern Gulf of Mexico: Multiple working hypotheses. *Estuaries* **1997**, *20*, 1–13. [CrossRef]
17. Chabreck, R.H.; Joanen, T.; Palmisano, A.W. *Vegetation Type Map of the Louisiana coastal Marshes*; Louisiana Cooperative Wildlife Research Unit, Louisiana Wildlife and Fisheries Commission, and Louisiana State University: Baton Rouge, LA, USA, 1968.
18. Chabreck, R.H.; Linscombe, R.G. *Vegetation Type Map of the Louisiana coastal Marshes*; Louisiana Department of Wildlife and Fisheries: Baton Rouge, LA, USA, 1978.
19. Chabreck, R.H.; Linscombe, R.G. *Vegetation Type Map of the Louisiana coastal Marshes*; Louisiana Department of Wildlife and Fisheries: Baton Rouge, LA, USA, 1988.
20. Chabreck, R.H.; Linscombe, R.G. *Vegetation Type Map of the Louisiana coastal Marshes*; Louisiana State University and Louisiana Department of Wildlife and Fisheries: Baton Rouge, LA, USA, 1997.
21. Linscombe, R.G.; Chabreck, R.H.; Hartley, S. *Aerial Mapping of Marsh Dieback in Saline Marshes in the Barataria-Terrebonne Basins*; Biological Resources Division, Information and Technology Report; US Geological Survey: Washington, DC, USA, 2001.
22. Couvillion, B.R.; Barras, J.A.; Steyer, G.D.; Sleavin, W.; Fischer, M.; Beck, H.; Trahan, N.; Griffin, B.; Heckman, D. *Land Area Change in coastal Louisiana from 1932 to 2010*; U.S. Geological Survey Scientific Investigations Map 3164; US Geological Survey: Reston, VA, USA, 2011.
23. Swarzenski, C.M. *Surface-Water Hydrology of the Gulf Intracoastal Waterway in South-Central Louisiana, 1996–1999*; U.S. Geological Survey Professional Paper; US Geological Survey: Reston, VA, USA, 1672.
24. Chuang, W.S.; Wiseman, W.J. Coastal sea level response to frontal passages on the Louisiana-Texas shelf. *J. Geophys. Res. Oceans* **1983**, *88*, 2615–2620. [CrossRef]
25. Bloomfield, P. *Fourier Analysis of Time Series: An Introduction*; John Wiley: New York, NY, USA, 1976.
26. Large, W.; Pond, S. Open-ocean momentum flux measurements in moderate to strong winds. *J. Phys. Oceanogr.* **1981**, *11*, 324–336. [CrossRef]
27. Bendat, J.S.; Piersol, A.G. *Random Data: Analysis and Measurement Procedures*; John Wiley and Sons: New York, NY, USA, 1986.
28. Torrence, C.; Webster, P.J. Interdecadal changes in the ENSO-monsoon system. *J. Clim.* **1999**, *12*, 2679–2690. [CrossRef]
29. Jevrejeva, S.; Moore, J.C.; Grinsted, A. Influence of the Arctic oscillation and El Nino-southern oscillation (ENSO) on ice conditions in the Baltic Sea: The wavelet approach. *J. Geophys. Res.* **2003**, *108*, 4677. [CrossRef]
30. Daubechies, I. The wavelet transform, time-frequency localization, and frequency analysis. *IEEE Trans. Inf. Theory* **1990**, *36*, 961–1005. [CrossRef]
31. Kjerfve, B. Velocity averaging in estuaries characterized by a large tidal range to depth ratio. *Estuar. Coast. Mar. Sci.* **1975**, *3*, 311–323. [CrossRef]
32. Lerczak, J.A.; Geyer, W.R.; Chant, R.J. Mechanisms driving the time-dependent salt flux in a partially stratified estuary. *J. Phys. Oceanogr.* **2006**, *36*, 2296–2311. [CrossRef]
33. Preisendorfer, R.W. *Principal Component Analysis in Meteorology and Oceanography*; Elsevier: Amsterdam, The Netherlands, 1988.
34. Hearn, C.J.; Robson, B.J. On the effects of wind and tides on the hydrodynamics of a shallow Mediterranean estuary. *Cont. Shelf Res.* **2002**, *22*, 2655–2672. [CrossRef]
35. Gong, W.; Shen, J.; Cho, K.H.; Wang, H.V. A numerical model study of barotropic subtidal water exchange between estuary and subestuaries (tributaries) in the Chesapeake Bay during northeaster events. *Ocean Model.* **2009**, *26*, 170–189. [CrossRef]
36. Jia, P.; Li, M. Dynamics of wind-driven circulation in a shallow lagoon with strong horizontal density gradient. *J. Geophys. Res. Oceans* **2012**, *117*, C05013. [CrossRef]
37. Snedden, G.A.; Cable, J.E.; Wiseman, W.J. Subtidal sea level variability in a Mississippi River deltaic estuary. *Estuar. Coast.* **2007**, *30*, 802–812. [CrossRef]
38. Snedden, G.A. River, Tidal and Wind Interactions in a Deltaic Estuarine System. Ph.D. Thesis, Louisiana State University, Baton Rouge, LA, USA, 2006.

39. Garvine, R.W. A simple model of estuarine subtidal fluctuations forced by local and remote wind stress. *J. Geophys. Res. Oceans* **1985**, *90*, 11945–11948. [CrossRef]
40. Feng, X.; Li, C. Cold-front-induced flushing of the Louisiana Bays. *J. Mar. Syst.* **2010**, *82*, 252–264. [CrossRef]
41. Xia, M.; Xie, L.; Pietrafesa, L.J.; Whitney, M. The ideal response of a Gulf of Mexico estuary plume to wind forcing: Its connection with salt flux and a Lagrangian view. *J. Geophys. Res. Oceans* **2011**, *116*, C08035. [CrossRef]
42. Kobayashi, S.; Zenitani, H.; Nagamoto, K.; Futamura, A.; Fujiwara, T. Gravitational circulation and its response to the variation in river discharge in the Seto Inland Sea, Japan. *J. Geophys. Res. Oceans* **2010**, *115*, C03009. [CrossRef]
43. Cannon, G.A.; Holbrook, J.R.; Pashinski, D.J. Variations in the onset of bottom-water intrusions over the entrance sill of a fjord. *Estuaries* **1990**, *13*, 31–42. [CrossRef]
44. Holloway, P.E.; Symonds, G.; Nunes, V.R. Observations of circulation and exchange processes in Jervis Bay, New South Wales. *Aust. J. Mar. Freshw. Res.* **1992**, *43*, 1487–1515. [CrossRef]
45. deCastro, M.; Gomez-Gesteira, M.; Alvarez, I.; Prego, R. Negative estuarine circulation in the Ria of Pontevedra (NW Spain). *Estuar. Coast. Shelf Sci.* **2004**, *60*, 301–312. [CrossRef]
46. Alvarez, I.; deCastro, M.; Gomez-Gesteira, M.; Prego, R. Hydrographic behavior of the Galician Rias Baixas (NW Spain) under the spring intrusion of the Mino River. *J. Mar. Syst.* **2006**, *60*, 144–152. [CrossRef]
47. Garel, E.; Ferreira, O. Fortnightly changes in water transport direction across the mouth of a narrow estuary. *Estuar. Coast.* **2012**, *36*, 286–299. [CrossRef]
48. Geyer, W.R.; Cannon, G.A. Sill processes related to deep water renewal in a fjord. *J. Geophys. Res. Oceans* **1982**, *87*, 7985–7996. [CrossRef]
49. deMiranda, L.B.; deCastro, B.M.; Kjerfve, B.J. Circulation and mixing due to tidal forcing in the Bertioga Channel, Sao Paulo, Brazil. *Estuaries* **1998**, *21*, 204–214. [CrossRef]
50. Li, M.; Zhong, L. Flood-ebb and spring-neap variations of mixing, stratification and circulation in Chesapeake Bay. *Cont. Shelf Res.* **2009**, *29*, 4–14. [CrossRef]
51. Granat, M.A.; Richards, D.R. Chesapeak Bay physical model investigations of salinity response to neap-spring tidal dynamics: A descriptive examination. In *Estuarine Variability*; Wolfe, D.A., Ed.; Academic Press: New York, NY, USA, 1986; pp. 447–462.
52. Dyer, K.R. Mixing caused by lateral internal seiching within a partially mixed estuary. *Estuar. Coast. Shelf Sci.* **1982**, *15*, 443–457. [CrossRef]
53. Dyer, K.R.; New, A.L. Intermittency in estuarine mixing. In *Estuarine Variability*; Wolfe, D.A., Ed.; Academic Press: New York, NY, USA, 1986; pp. 321–340.
54. Chen, S.N.; Sanford, L.P. Axial wind effects on stratification and longitudinal salt transport in an idealized, partially mixed estuary. *J. Phys. Oceanogr.* **2009**, *39*, 1905–1920. [CrossRef]